LCLS-II Technical Note

SXRSS performance with thermal heating of the grating

LCLS-II-TN-21-04

(Jun. 2021, R1.0)

Erik Hemsing, Lin Zhang, Jacek Krzywinski

(SLAC)

The high repetition rate LCLS-II FEL x-ray beam incident on the SXRSS grating surface causes heating that leads to a thermal deformation. If large enough, the deformation can significantly modify the optical transport properties through the system and negatively impact the self-seeding performance. Here we examine the effects of a static deformation on the performance for different incident average x-ray power, different photon energies, and for different cooling schemes. We find that simple braided strap cooling is sufficient to maintain nominal SXRSS operations at full repetition rate if the incident average FEL power is kept below 3 W.

I. INTRODUCTION

The soft x-ray self-seeding system (SXRSS) at the the LCLS free electron laser (FEL) was designed and implemented to reduce the x-ray bandwidth and increase the x-ray spectral brightness delivered to experiments needing high photon energy resolution [1, 2]. The system has been ported and upgraded for use on the LCLS-II SXR undulator line to provide similar capabilities with the high repetition rate ($\leq$1 MHz) beam.

To prevent multi shot damage to the Pt-coated SXRSS grating, the incident x-ray pulse fluence is kept below 30 mJ/cm^2, which broadly translates to 1-5 μJ/pulse if the nearest upstream undulator (U9) is in-out [3]. At the full 1 MHz repetition rate of the LCLS-II SC linac, this produces 1-5 W of average x-ray beam power incident on the SXRSS grating surface. This is high enough to cause heating that leads to a thermal deformation which modifies the sensitive imaging properties of the dispersed beam. Here we show that below 3 W, the impact on the seeding system performance is minor and tolerable across the full SXRSS tuning range of 250-1240 eV. Approaching 5 W leads to a precipitous decrease in the resolving power for photon energies >750 eV, but is still tolerable for lower photon energies.

We also consider average power levels exceeding 5 W that can reach up to 25 W at high photon energy. This is an effort to understand the system tolerance to higher incident fluences as afforded by B4C coated gratings under consideration that have a higher damage threshold. In a separate set of studies [4], simulations indicate that the B4C coated grating exhibits the best performance with respect to maximum seeding power limited by the damage, especially for photon energies larger than 750 eV. At 1200 eV, the B4C coated grating should allow an incident x-ray pulse one order of magnitude higher than that for the Pt coated grating. At the lower photon energy range, 400 eV-700 eV, the incident pulse can be 2-3 times higher, but the overall performance of B4C and Pt gratings is comparable because the efficiency of the B4C grating is 2-3 times lower than the Pt grating. Thus, a B4C coated grating should allow 2-10 times higher incident pulse fluences across the SXRSS tuning range while providing up to 3 times more seed power at higher photon energies to improve the SXRSS performance. Accordingly, we find from the studies presented here that average incident powers up to 10 W can be used without a significant decrease in resolving power, but only for photon energies $\leq$750 eV and only if U9 is "out" (i.e., not contributing to FEL gain). Above this level, the thermal distortion can significantly reduce both the resolving power and, at high photon energies, the seed power coupling to the electron beam in the downstream undulator.

II. SXRSS SEEDING AND IMAGING

As shown in FIG. 1, the optical transport of the SXRSS is designed as an imaging system to isolate a narrow spectral portion of the incoming SASE spectrum into the downstream undulators for FEL amplification. The compact design with unclosed optical dispersion makes it sensitive to variations in the optical transport, either from upstream or within the device. The incident SASE pulse is dispersed and focused by the torodial grating surface, which has a radius of curvature $R_1 = 185$ m in the tangential (horizontally dispersed) plane and $\rho = 0.18$ m in the sagittal (vertical) plane. In the horizontal plane, the pulse comes to a waist for the center photon energy close to the slit, which is then imaged by the M2 mirror into the downstream undulator. In the vertical plane, the focusing is purely from the grating. The slit nominally helps to isolate the frequencies of interest for amplification, but in practice, the

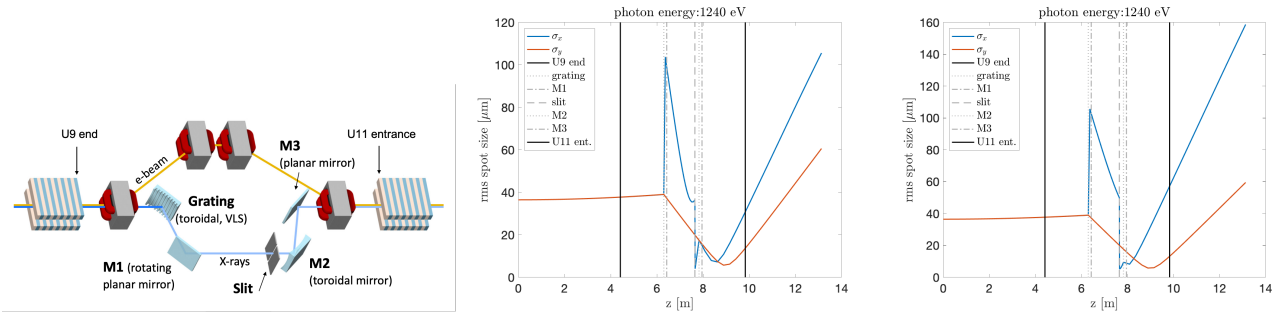

FIG. 1: Left: Layout of the SXRSS system (not to scale). The spot size of a monochromatic x-ray beam evolves through the SXRSS system under normal conditions (center) and with a $h = 250$ nm high thermal bump from 25 W of incident average power on the grating surface (right). The bump counteracts the focusing from the toroidal grating surface and spoils the dispersive-plane imaging into the downstream undulator. The horizontal spot size after the grating is scaled by $\sin\theta_d/\sin\theta_i$ where θ_d and θ_i are the angles of diffraction and incidence, respectively.

finite width of the electron beam ($\approx 30\mu$m) over the few-meter interaction length in the downstream undulator serves to define the nominal resolving power R_p and seed power P_s of the system. Absent a thermal deformation, the design specifies a FWHM resolving power of $R_p = \omega_0/\Delta\omega$=5000-8000 and peak seed power of around P_s=20-40 kW (the average shot noise power is roughly 200-350 W), depending on the photon energy.

III. THERMAL DEFORMATION MODELING

Thermal deformation simulations were performed using an input set of x-ray pulse parameters from LCLS-II FEL simulations. X-ray pulse parameters are given in Table I and represent an aggressive set of SASE pulses from the U8 undulator (i.e., U9 is out) for the FEL electron beam parameters given in Table III. In particular, the incident x-ray pulse energies exceed the nominal 5 μJ/pulse set point for the Pt coated grating in anticipation of operating at higher incident fluxes with the B4C grating with undulator U9 out. A Gaussian power distribution on the grating ruled area (20x4 mm) was assumed, given the expected spot sizes of SASE FEL radiation on the grating and including the $\theta_i = 1.04$ degree angle of incidence. Because the power density of the spontaneous radiation is much smaller than the FEL pulse, and because the majority of the spontaneous radiation hits the chin guard (or slit) and shield, it can be neglected.

We start with numerical simulations of the induced heating assuming cooling by a braided copper strap attached to the side of the grating. Thermal radiation cooling effects are also included. The strap is the simplest cooling approach, and turns out to be sufficient for baseline operations. Alternate cooling schemes were also examined, as described in Sec. V. In all cases, the heating-induced deformity was then used in a Fourier propagation code of the full SXRSS system to appraise the optical transport and seeding characteristics.

Figure 2 shows the shape and size of the heating-induced surface bumps at full rep-rate for different photon energies using the parameters in Table I, and assuming strap cooling. The bump acts to defocus the x-ray beam by counteracting the grating curvature, effectively increasing both R_1 and ρ. This pushes the focus downstream of the slit and closer to $M2$ such that $M2$ no longer correctly images the slit. As seen in FIG. 1, for large thermal bumps $M2$ can no longer focus the beam into the downstream undulator, and the seed power drops significantly. The distortion on the wavefront caused by the Gaussian-like bump also reduces the resolving power of the seed at the highest powers

TABLE I: X-ray and grating parameters used for deformation simulations

Photon energy [eV]	**250**	**750**	**1240**
Pulse Energy [μJ]	6.4	9.1	24.6
rms spot size on grating, (x, y) [mm]	5.785, 0.105	2.589, 0.049	2.039, 0.039
Pulse Fluence [mJ/cm^2]	9.4	63	270
Ave. power @ 1 MHz [W]	6.4	9.1	24.6

TABLE II: FEL parameters

E [GeV]	4
Q [pC]	100
I [kA]	1
β [m]	18
ϵ_n [mm mrad]	0.35

and photon energies (See Sec. IV).

The effect of the bump can be roughly approximated in the linear theory by calculating the bump radius of curvature and comparing it to the intrinsic radius of curvature on the grating for focusing. Though this approximation is not used in the full transport simulations (See Sec. IV), it provides an order of magnitude assessment of the impact of the bump on the focusing. Assume the bump is a 2D Gaussian-shaped distortion on the grating surface with horizontal and vertical rms spot sizes Σ_x and Σ_y. To lowest order, the radius of curvature in each dimension due to a dimple of height h is then $R_{x,y} = -\Sigma_{x,y}^2/h$. The negative sign indicates the defocusing effect for a bump. In the linear transport theory approximation, these radii add inversely to the intrinsic tangential R_1 and sagittal ρ grating surface radii of curvature to yield the total effective radii of curvature in each dimension. Figure 3 shows how the induced bump radius of curvature and bump height vary with incident average power at the grating, which can be related directly to the repetition rate from Table I. For the same incident power, the higher photon energies produce taller bumps, which we will see means that they are more strongly impacted from the standpoint of seeding performance. The curves in Fig. 3 show that the bump radius of curvature in the vertical dimension is negligible compared to the intrinsic radius of curvature ρ on the grating surface. However, the curvature in the horizontal dimension becomes comparable to R_1 (though opposite in sign) when the incident average power approaches 10 W at 1240 eV. At this point the horizontal focusing is lost and the optical imaging no longer serves its function in the dispersive plane as shown by comparison of the optical transport in Fig. 1.

IV. X-RAY TRANSPORT SIMULATIONS

To quantify the effect of the bump on the system performance the bump surface distributions from the thermal simulations were fitted to smooth functions of grating surface height deformation $z_B = f(x, y)$ (see Fig. 2) and used in a Fourier optical transport code [5]. This enabled the changes in resolving power and seed power to be calculated to arbitrary optical order, i.e., not restricted to simple spherical aberrations, for example. From grating theory, the

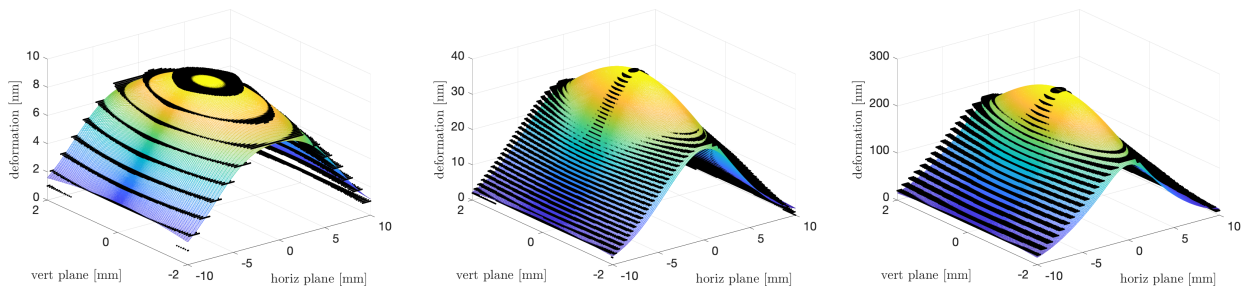

FIG. 2: Deformations from simulations at full rep rate for 250 eV (left), 750 eV (middle) and 1240 eV (right) using the parameters in Table I. Black dots are from numerical heating simulations, and the surfaces are fits used in the Fourier x-ray propagation code.

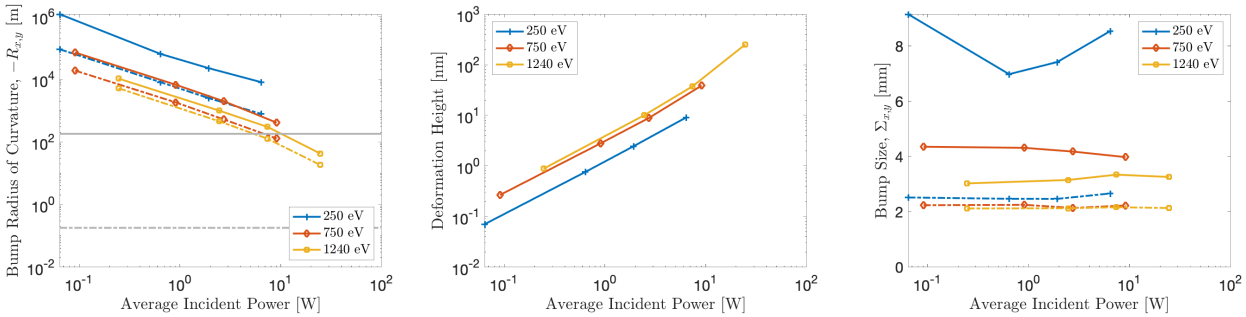

FIG. 3: Thermal bump radius of curvature $R_{x,y}$ (left), height h (center), and size $\Sigma_{x,y}$ (right) on grating surface vs average incident power using Table I for different repetition rates. The horizontal plane values are solid lines, the vertical are dashed lines. Strap cooling is assumed. For comparison, the nominal horizontal $R_1 = 185$ m (solid gray) and vertical $\rho = 0.18$ m (dashed, gray) radii of curvature on the grating surface are also shown. The horizontal (x) radius of curvature of the bump is equal and opposite to R_1 at 1240 eV once the power reaches about 10 W, which effectively cancels the toroidal grating shape. In contrast, the vertical focusing (dashed lines) is essentially unchanged throughout, as $\rho \ll -R_y$.

phase introduced on the x-rays by the bump is

$$\Delta\Phi_B = kz_B \left[\frac{z_B}{2} \left(\frac{1}{r_1} + \frac{1}{r_2} \right) - (\sin\theta_d + \sin\theta_i) \right] \tag{1}$$

where r_1 is the distance from the SASE source to the grating, and r_2 is the distance from the grating to the slit. (Note, expanding $z_B = f(x, y)$ to second order in x, y allows one to identify the approximate bump radii of curvature from $z_B \approx h + x^2/2R_x + y^2/2R_y$.)

Three different sets of optical transport simulations were conducted to cover the potential variety of input SASE pulses on the grating and to capture the sensitivity of the SXRSS system to the optical transport. For simplicity here we only consider idealized single mode beams with M^2=1, whereas the actual incoming SASE pulses may be

TABLE III: X-ray waist sizes and source points for the Fourier transport simulations.

Photon energy [eV]	**250**	**750**	**1240**
SASE U8 (w_0 [μm], r_1 [m])	(204, 6.3)	(91, 6.3)	(73, 6.3)
Ideal U8 (w_0 [μm], r_1 [m])	(49, 7.15)	(40, 8.0)	(37, 8.7)
Ideal U9 (w_0 [μm], r_1 [m])	(49, 2.75)	(40, 3.6)	(37, 4.3)

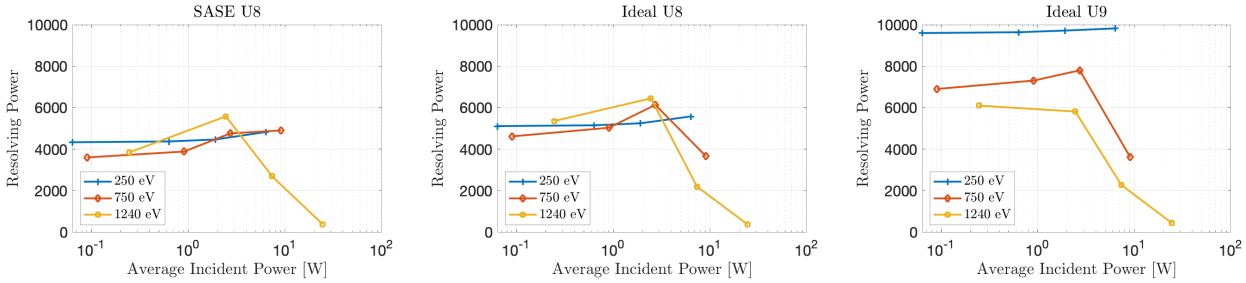

FIG. 4: Simulated seed resolving power as a function of average power for a transversely large SASE beam from U8 (left), a smaller ideal beam from U8 (middle), and the same ideal beam from U9 (right).

multi-moded with $M^2 \approx 3-4$. While these beams can also be modeled, the beam is strongly dispersion-dominated after the grating, which is what determines most of the salient features of the SXRSS system (such as resolving power). The parameters for the three cases are shown in Table III. They differ only in the source point and initial spot size, and are dubbed SASE U8, Ideal U8, and Ideal U9 [9]. In each case, the input beam was modeled as a simple Gaussian beam transversely and in frequency (using a $\sigma_\omega/\omega = 0.1\%$ relative bandwidth SASE pulse) to model the average over many SASE shots. The SASE U8 parameters are extracted from full Genesis simulations of a beam emitted from U8 [6]. These are the same parameters used to produce the illumination on the grating for the thermal bump calculations in Table I. In the SASE U8 case, the guided FEL "supermode" has not fully developed, so the x-ray beam has a somewhat large spot size and multiple transverse modes each shot. For simplicity, we model the shot-to-shot average of this by a large but single transverse Gaussian mode. The other beams, Ideal U8 and Ideal U9, both derive their spot sizes and source points (within U8 or U9, respectively) assuming the high-gain FEL supermode has developed. In this case, the spot size and radius of phasefront curvature at the undulator exit can be approximated from 3D FEL theory as [7]

$$w = 2\sigma_x \left(\frac{L_{3D}}{2k\sigma_x^2}\right)^{1/4}, \qquad R_c = -1.86 L_{3D} \left(\frac{L_{3D}}{2k\sigma_x^2}\right)^{-1/2} \tag{2}$$

where $\sigma_x = \sqrt{\epsilon_n \beta/\gamma}$ is the rms transverse electron beam size, $\lambda = 2\pi/k$ is the wavelength, and L_{3D} is the 3D power gain length using the Xie fit [8] and including 1.0 m drifts between undulator sections. The waist size w_0 and the source point inside the undulator z_s are then calculated directly by back-propagating with $w_0^2 = \frac{4R_c^2 w^2}{4R_c^2 + k^2 w^4}$ and $z_s = w_0^2 \frac{k^2 w^2}{4R_c}$. The undulator sections are 3.3 m, and the distance from the end of U9 to the grating is 1.883 m, so the source point is $r_1 = 1.883 - z_s$ =2.75 to 8.7 m depending on the energy and if U9 is inserted.

Figure 4 shows the resolving power as a function of incident average power for the three different optical input sets. The resolving power is calculated by integrating the diverging/dispersed radiation over a volume in the downstream U11 undulator that mimmicks the overlap of the radiation with the electron beam. In all three cases, the resolving power at low photon energy (250 eV) is essentially independent of the rep rate/average power, while at high photon energy the resolving power shows a marked decrease once the power reaches roughly 3 W. We therefore chose 3 W as the maximum average power level for the SXRSS system at LCLS-II to broadly cover the full tuning range of photon energies, though accommodations can be made to reach up to 10 W for $\leq$ 750 eV. Interestingly, if the Ideal U9 beam can be achieved in practice, these simulations suggest a significant improvement in resolving power for low to modest incident power compared with source positions within U8.

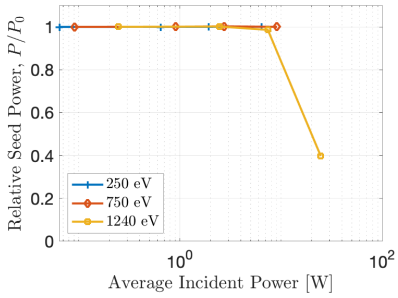

FIG. 5: Seed power in the U11 undulator vs incident average power. The seed power is normalized to the value at low rep rate where there is no thermal bump. This is for the ideal beam emitted from U8, but results with the SASE U8 beam and ideal U9 beams are essentially identical.

It is interesting to note that, in some cases, the resolving power actually increases with the thermal deformation. This is because the system was designed to accommodate a large tuning range, so for some photon energies the imaging properties that define the seed bandwidth are not optimized. In these cases, the defocusing effect of the bump can actually improve the imaging into U11.

The impact of the bump deformation on the seed power reaching the electron beam was also studied, and the results are shown in Fig. 5. Results were nearly identical for the SASE U8, Ideal U8, and Ideal U9 cases, so only one is shown. We find that the seed power, again integrated over the electron beam volume in U11, is essentially unaffected by the bump *except* at high photon energy and for > 10 W.

V. ADDITIONAL COOLING

The effects of improved grating cooling schemes were also examined and compared with cooling with the braided strap. Figure 6 shows the deformation thermal heating simulation results for the braided strap, active water cooling, and cryo (LN) cooling on side of the grating at 1 MHz for 1240 eV. Active side water cooling is up to three times better than braided strap cooling in terms of the height of the deformation, and liquid nitrogen cooling can be 100 times better. In fact, cyro-cooling with LN produces a dimple rather an a bump. This is because the thermal expansion coefficient of the silicon substrate goes to negative below 125 K, so it contracts when heated by the absorbed FEL power. Therefore the deformation on the grating surface is becomes concave instead of convex, and adds a slight but overall negligible focusing.

Figure 7 shows the results of Fourier transport simulations of the x-rays at 1 MHz for the different cooling schemes. The resolving power is shown, and is normalized with the resolving power with zero deformation. The cryo cooling scheme, which results in tiny deformations less than 2 nm deep, preserves the baseline resolving power across the full energy tuning range up to the full rep rate, as expected. Strap cooling and water cooling result in nearly the same resolving power performance at the low and high energies, but water cooling leads to better performance in the mid range tuning energies. Given the complexity of adding either water cooling or cryo cooling, it appears that strap cooling is sufficient for operations below 3 W.

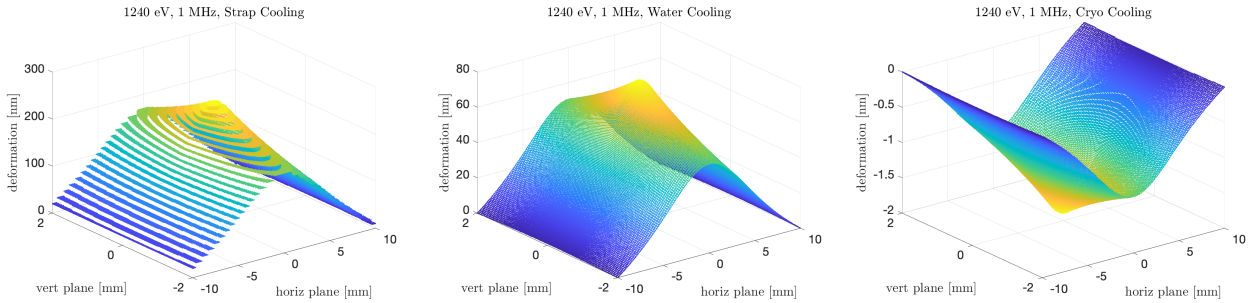

FIG. 6: Simulated deformations at full rep rate for different cooling schemes at 1240 eV.

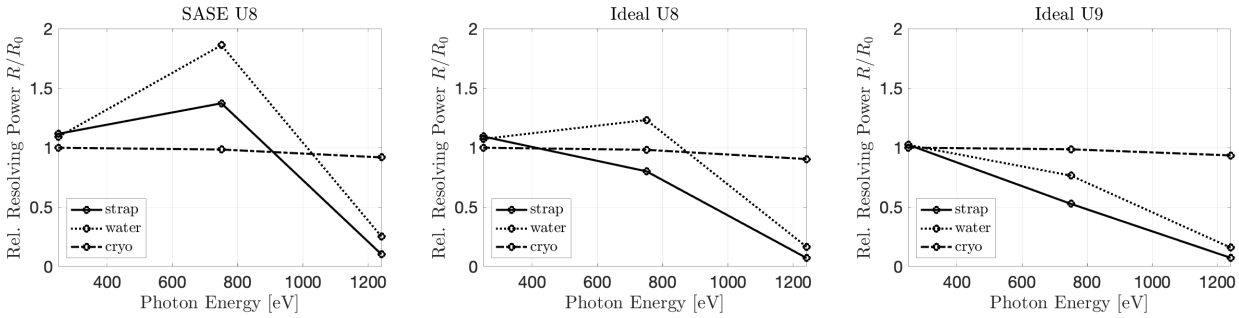

FIG. 7: Relative resolving power at full rep rate for different cooling schemes, with different input x-ray beams. The resolving power is normalized to the value at low rep rate where there is no thermal bump.

VI. SUMMARY

We have modeled the thermal deformation of the SXRSS grating surface at different photon energies and average input powers, and included the deformation in simulations of the x-ray transport through the SXRSS system. We find that strap cooling is sufficient to preserve baseline operations in terms of resolving and seed power if the average input power is kept below 3 W. Clamped water cooling can lower the temperature on the grating when running at MHz, and reduce slightly the thermal deformation of the grating. Liquid nitrogen cooling can significantly reduce the thermal deformation to negligible level, though at the expense of complexity.

[1] D. Ratner, R. Abela, J. Amann, C. Behrens, D. Bohler, G. Bouchard, C. Bostedt, M. Boyes, K. Chow, D. Cocco, et al., Phys. Rev. Lett. **114**, 054801 (2015), URL https://link.aps.org/doi/10.1103/PhysRevLett.114.054801.

[2] D. Cocco, R. Abela, J. W. Amann, K. Chow, P. J. Emma, Y. Feng, G. L. Gassner, J. Hastings, P. Heimann, Z. Huang, et al., in *X-Ray Lasers and Coherent X-Ray Sources: Development and Applications X*, edited by A. Klisnick and C. S. Menoni, International Society for Optics and Photonics (SPIE, 2013), vol. 8849, pp. 31 – 38, URL https://doi.org/10.1117/12.2024402.

[3] J. Krzywinski, R. Conley, S. Moeller, G. Gwalt, F. Siewert, C. Waberski, T. Zeschke, and D. Cocco, Journal of Synchrotron Radiation **25**, 85 (2018), URL https://doi.org/10.1107/S1600577517016083.

[4] J. Krzywinski, SLAC Technical Note I-120-203-031-00 (2021).

[5] S. Serkez, J. Krzywinski, Y. Ding, and Z. Huang, Phys. Rev. ST Accel. Beams **18**, 030708 (2015), URL https://link.aps.org/doi/10.1103/PhysRevSTAB.18.030708.

[6] G. Marcus, SLAC Physics Requirements Document LCLSII-3.2-PR-0101-R0 (2014).

[7] E. Hemsing, Ph.D. thesis, University of California Los Angeles (2011).

[8] M. Xie, Nuclear Instruments and Methods in Physics Research A **445**, 59 (2000).

[9] A fourth set, SASE U9, using an identical large beam originating from U9 was also studied, but the results were identical with SASE U8